


Ultrafast Acoustofluidic Exfoliation of Stratified Crystals

Heba Ahmed, Amgad R. Rezk, Benjamin J. Carey, Yichao Wang, Md Mohiuddin, Kyle J. Berean, Salvy P. Russo, Kourosh Kalantar-zadeh,* and Leslie Y. Yeo*

While the remarkable properties of 2D crystalline materials offer tremendous opportunities for their use in optics, electronics, energy systems, biotechnology, and catalysis, their practical implementation largely depends critically on the ability to exfoliate them from a 3D stratified bulk state. This goal nevertheless remains elusive, particularly in terms of a rapid processing method that facilitates high yield and dimension control. An ultrafast multiscale exfoliation method is reported which exploits the piezoelectricity of stratified materials that are noncentrosymmetric in nature to trigger electrically-induced mechanical failure across weak grain boundaries associated with their crystal domain planes. In particular, it is demonstrated that microfluidic nebulization using high frequency acoustic waves exposes bulk 3D piezoelectric crystals such as molybdenum disulphide (MoS_2) and tungsten disulphide (WS_2) to a combination of extraordinarily large mechanical acceleration ($\approx 10^8 \text{ m s}^{-2}$) and electric field ($\approx 10^7 \text{ V m}^{-1}$). This results in the layered bulk material being rapidly cleaved into pristine quasi-2D-nanosheets that predominantly comprise single layers, thus constituting a rapid and high throughput chip-scale method that opens new possibilities for scalable production and spray coating deposition.

Relying on the weak out-of-plane van der Waals forces between horizontal planes of transition metal dichalcogenides (TMDs),^[1] existing high-yield exfoliation techniques employ liquid phase sonication approaches with the aid of appropriate solvents as stabilizing agents.^[2–5] These processes are, however, rather lengthy, typically requiring days to achieve commercially acceptable yields. Chemical exfoliation methods involving ion intercalation followed by ultrasonication have also been explored, although the introduction of intercalating agents can lead to phase changes,^[6] atomic substitutions,^[7] or line defects,^[8] which often compromise the overall quality of the crystal.^[8]

H. Ahmed, Dr. A. R. Rezk, Dr. B. J. Carey, Dr. Y. Wang, Md Mohiuddin, Dr. K. J. Berean, Prof. K. Kalantar-zadeh, Prof. L. Y. Yeo
School of Engineering
RMIT University
Melbourne, VIC 3000, Australia
E-mail: kourosh.kalantar@rmit.edu.au; leslie.yeo@rmit.edu.au
Prof. S. P. Russo
Australian Research Council Centre of Excellence in Exciton Science
School of Science
RMIT University
Melbourne, VIC 3000, Australia

 The ORCID identification number(s) for the author(s) of this article can be found under <https://doi.org/10.1002/adma.201704756>.

DOI: 10.1002/adma.201704756

The recent discovery of the piezoelectric nature of noncentrosymmetric materials with *odd* numbers of layers^[5] offers an interesting possibility to exploit a combination of both mechanical and electric fields to drive failure across planes of stratified crystals such that the material is cleaved into single- or few-layer quasi-2D-nanosheets. To take advantage of this piezoelectric property that is possessed by 2D TMDs, we expose a suspension comprising bulk 2H MoS_2 and WS_2 to the large mechanical and electric stresses inherent in a microfluidic nebulization process driven by high frequency (10 MHz order) acoustic excitation. These novel hybrid surface and bulk acoustic waves (HYbriD Resonant Acoustic (HYDRA)),^[9] or their surface acoustic wave precedent, have been shown to be very efficient nebulization platforms for drug delivery and nanoparticle synthesis, among other applications.^[10–12] In this work, we provide the

first demonstration of its use for continuous ultrafast exfoliation of stratified TMD crystals, which are efficiently cleaved down to single- or few-layer quasi-2D-nanosheets—in stark contrast to their centrosymmetric counterparts such as graphite, which we show to be insensitive to the electric field contribution. The method's potential for high throughput processing can also be exploited given the low cost and scalability of the miniature chip-scale device through massive parallelization.

As illustrated in **Figure 1a,b**, liquid suspensions of bulk MoS_2 or WS_2 dispersed in water are drawn from a reservoir through a short wick onto the HYDRA device, which comprises a piezoelectric chip on which interdigitated transducer electrodes are patterned via standard lithographic techniques (see the Experimental Section). They immediately nebulize upon contact to produce a mist of micrometer-dimension aerosol droplets upon excitation of the hybrid acoustic waves on the device. The liquid transport and its subsequent nebulization can be attributed to the large mechanical acceleration ($\approx 10^8 \text{ m s}^{-2}$) on the surface of the device associated with the 10 MHz order traveling acoustic waves that propagate along it.^[10] Simultaneously, exposure of the bulk TMDs to these large mechanical stresses, and the corresponding electrical field associated with the electromechanical coupling within the noncentrosymmetric TMDs during nebulization, results in their exfoliation to produce quasi-2D-nanosheets, which are dispersed within the aerosol droplets and subsequently collected as the droplets deposit onto a collector plate mounted above the device (**Figure 1a**).

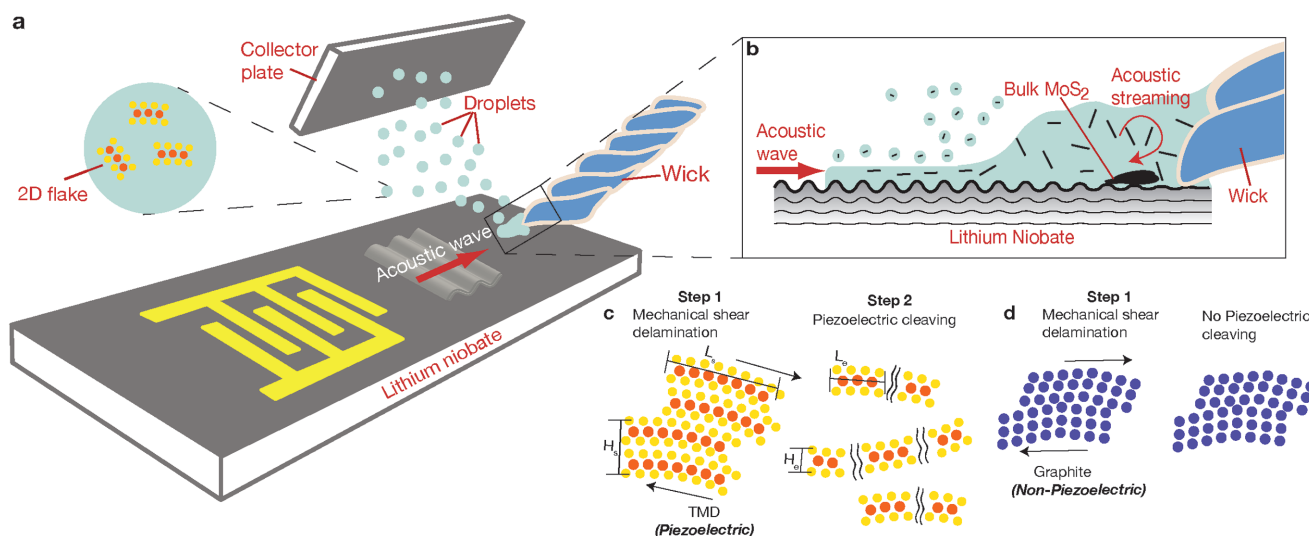


Figure 1. a) Schematic illustration of the HYDRA device for the exfoliation of quasi-2D materials. Upon excitation of the acoustic wave on the device, the pre-exfoliated feedstock solution comprising the bulk MoS_2 , WS_2 , or graphite suspension is drawn from the reservoir to the edge of the device via a wick where it is immediately nebulized. The MoS_2 , WS_2 , or graphite flakes that are exfoliated in the process are encapsulated in the aerosol droplets that ensue, and are collected for further characterization when the droplets deposit onto the collector plate. b) Magnification of the schematic showing the liquid meniscus and thin front-running film that forms as a consequence of the acoustic wave excitation,^[14,17] from which nebulization occurs. c) Schematic depiction of the multiscale mechanism that underpins the exfoliation process. The 3D bulk material first breaks down into intermediate flake structures with lateral dimensions L_s and thicknesses H_s through a mechanical delamination process as a consequence of the large shear stresses arising due to acoustic streaming in the liquid. Subsequently, the large electric field that accompanies the acoustic wave incites mechanical vibration in the intermediate structures if they are piezoelectric, which drives fracture of the flakes along the grain boundaries associated with the crystal domains such that they are cleaved into quasi-2D-nanosheets with lateral dimensions L_e and thicknesses H_e . d) For nonpiezoelectric materials such as graphite, only the mechanical shearing step occurs such that the final structures that are produced are the intermediate flakes with length L_s and thickness H_s .

Close inspection of the material obtained under high electric field intensities of 10^7 V m^{-1} via atomic force microscopy (AFM) reveals MoS_2 and WS_2 nanosheets that are typically $L_e \sim O(10 \text{ nm})$ in lateral dimension and $H_e \sim O(1 \text{ nm})$ in thickness (Figure 2a,b,d,e). The high resolution transmission electron microscopy (HRTEM) images in Figure 2c,f indicate that these quasi-2D-nanosheets possess high crystallinity, evidenced by the parallel and ordered lattice fringes with 0.27 nm average spacing, corresponding to the (100) lattice plane of MoS_2 and WS_2 .^[13] This is further confirmed by both Raman and UV–vis spectroscopic characterization of the nanosheets (Figures S1 and S2, Supporting Information), the powder X-Ray diffraction (XRD) data in Figure S3 (Supporting Information), and the experimental data showing the number of layers that make up each nanosheet in Figure 3p (see also Figure S4p, Supporting Information), inferred from the AFM measurements of their individual thicknesses which show the majority of exfoliated nanosheets existing as monolayers.

As illustrated schematically in Figure 1c, we postulate a multiscale mechanism responsible for the exfoliation. 3D bulk stratified crystals are first delaminated under mechanical shear into intermediate structures with characteristic length and thickness scales, L_s and H_s , respectively, akin to those observed in shear exfoliation processes carried out in rotary mixers and sonicators. The large shear stresses here—on the order 10^4 s^{-1} —arise, however, as a consequence of the intense acoustic streaming that is induced in the liquid meniscus during the nebulization process, as schematically illustrated

in Figure 1b;^[14] such large shear rates being a consequence of the unprecedented $O(10^8 \text{ ms}^{-2})$ surface acceleration associated with the acoustic waves.^[10] Further reduction of this intermediate state into thinner 2D structures of thicknesses H_e with smaller lateral dimensions L_e subsequently occurs. This can be attributed to the strong mechanical vibration acting at the end planes of the flakes, enhanced by the inherent electric field associated with the electromechanical coupling of the acoustic wave in nanosheets with odd numbers of layers due to their intrinsic piezoelectricity.

The delamination step of the bulk crystals under mechanical shear is evident when graphite—a *centrosymmetric* material and hence one that is nonpiezoelectric, unlike MoS_2 , WS_2 , and other TMDs—is exfoliated (Figure 1d). It can be seen that only larger and thicker graphite flakes with dimensions $L_s \approx 100 \text{ nm}$ and $H_s \approx 7\text{--}9 \text{ nm}$ (minimum) are produced (Figure 2g–i; Figure S5, Supporting Information); there is no further piezoelectric reduction of these flakes into the smaller and thinner nanosheets that were obtained for the cases of MoS_2 and WS_2 . This is confirmed by the powder XRD data in Figure S3 (Supporting Information) where the characteristic graphite peak is observed, in contrast to the data for exfoliated MoS_2 and WS_2 in which the characteristic peaks associated with the (002) planes are evident. Large intermediate flakes with similar dimensions to those for graphite are also observed for piezoelectric MoS_2 and WS_2 when the subsequent piezoelectric reduction step is suppressed by depositing a thin metallic screening layer to eliminate a large proportion of the electric field (Figure 3a–d).

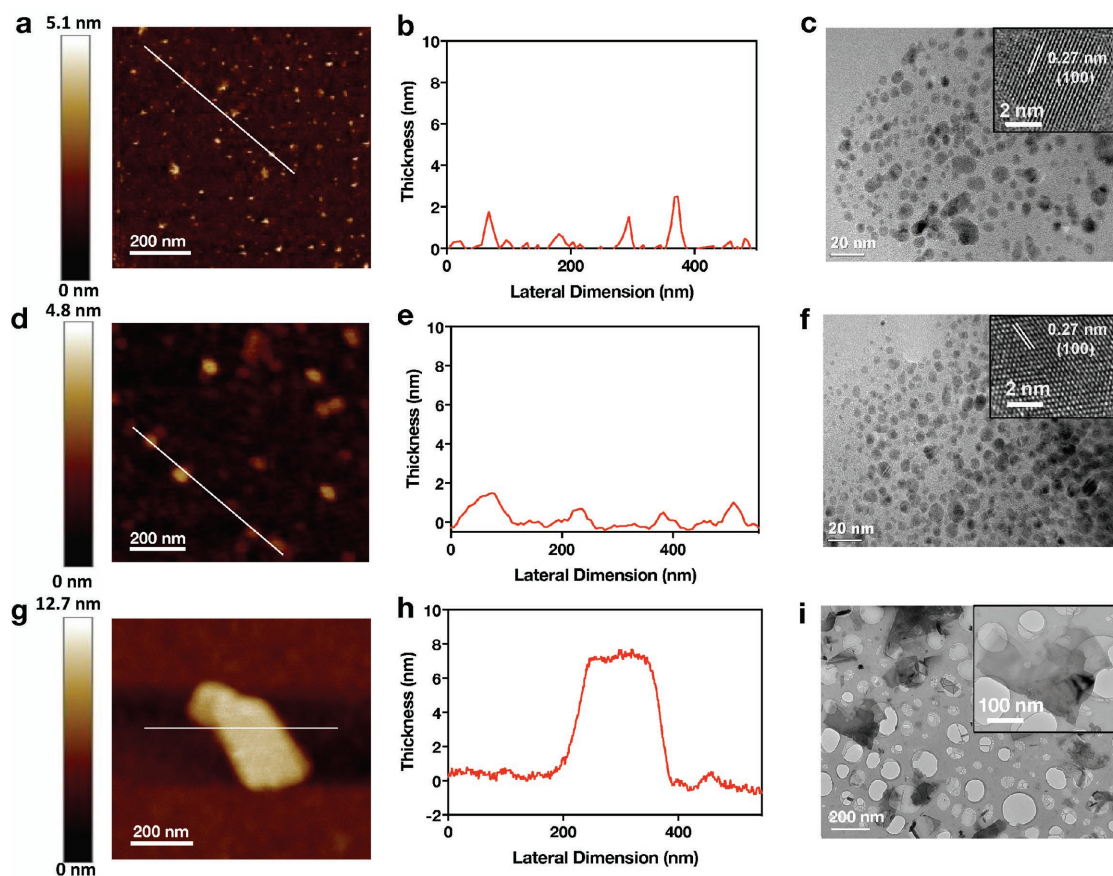


Figure 2. a,d,g) AFM scans, b,e,h) corresponding thickness measurements, and c,f,i) HRTEM images of the structures produced under acoustofluidic exfoliation with the HYDRA device. The top (panels a–c) and middle (panels d–f) rows correspond to the data for MoS₂ and WS₂, respectively, both of which are inherently piezoelectric when existing with odd numbers of layers. The bottom row (panels g–i) corresponds to the data for graphite, which is nonpiezoelectric.

We subsequently proceeded to vary the electric field intensity to elucidate its role in the subsequent piezoelectric exfoliation step. It can be seen that an increasing number of smaller single- and few-layer quasi-2D-nanosheets are progressively produced as the electric field intensifies, as seen in Figure 3. More specifically, the bimodal distribution in the lateral flake dimension can be seen to eventually disappear at large electric fields (Figure 3c,g,k,o). Their final dimension L_e , which is commensurate with typical 10–30 nm MoS₂ and WS₂ domain sizes reported in the literature^[15] and the 11.9 nm average crystallite size measured via powder XRD (Figure S3, Supporting Information), suggests that the intermediate structures are cleaved laterally along weak fracture planes defined by the crystal grain dislocation boundaries of the nanosheets, as schematically illustrated in Figure 1c. Concurrently, the numbers of layers of the nanosheets are observed to decrease with increasing electric field intensity as the piezoelectric cleaving progressively thins the intermediate flakes down towards the monolayer limit (Figure 3d,h,l,p). Interestingly, we note that the optimum condition for which the highest number of monolayers is obtained occurs at $\approx 10^6$ V m⁻¹ (Figure 3l). Beyond this threshold value, the high field intensity results in the intense reduction in the lateral dimension of the flakes, giving rise to small nanosheets with

profound metal edge boundaries that are likely to weaken the inherent piezoelectricity of the material, thereby decreasing the likelihood of further thinning. As such, we observe the relative number of monolayers to slightly decrease as the electric field intensity is increased from 10^6 to 10^7 V m⁻¹ (Figure 3l,p).

To verify our hypothesis of the central role that the electric field plays in the piezoelectric reduction step, spin-dependent hybrid density functional theory calculations were employed to predict the probability of exfoliating an MoS₂ slab comprising seven layers under an applied electric field of 10^6 V m⁻¹. We observe in Figure 4a good qualitative agreement between the theoretical prediction and the experimental observations under similar conditions (e.g., the same electric field intensity), not just in terms of the observed tendency to produce nanosheets with odd numbers of layers, but also the dominance of single-layer nanosheets in addition to the decreasing probability of nanosheets with larger numbers of layers.

In summary, we have demonstrated a novel solvent-free exfoliation method for rapidly synthesizing single- and few-layer quasi-2D-nanosheets of MoS₂ and WS₂ (and, more generally, those of TMDs) from their 3D stratified bulk, with the possibility of control over the size distribution of the nanosheets simply by adjusting the electric field intensity, as seen in

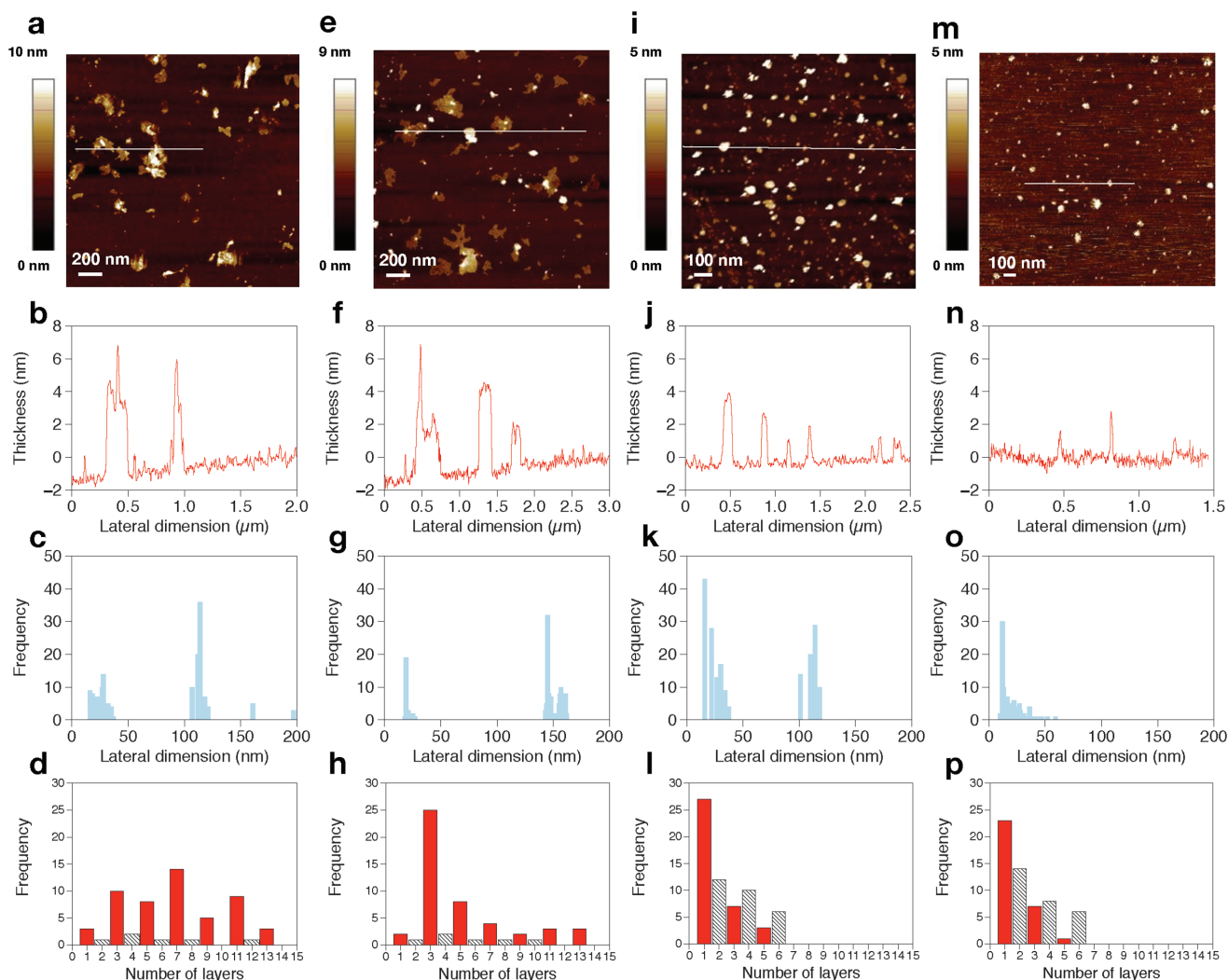


Figure 3. a,e,i,m) AFM scans, b,f,j,n) corresponding thickness measurements, c,g,k,o) lateral size frequency distributions, and d,h,l,p) frequency distributions of obtaining a 2D MoS_2 nanosheet with n numbers of layers under varying electric field intensities. First column (panels a–d): weak electric field due to the presence of a thin metallic screening layer atop the device; second column (panels e–h): 10^5 V m^{-1} ; third column (panels i–l): 10^6 V m^{-1} ; fourth column (panels m–p): 10^7 V m^{-1} .

Figure 3. The overall yield (mass ratio of the nanosheets to the bulk material) was found to be $\approx 2\%$, of which about 41% consisted of monolayers. Around $92\% \pm 2.39\%$ of MoS_2 is recovered postnebulization from which we estimate a production rate of $0.054 \text{ mg min}^{-1}$ given the rapid millisecond timescale of the nebulization process at rates of several mL min^{-1} .^[9] As this production rate—with just a single chip-scale device—is comparable to those reported for large scale industrial mixers,^[16] the possibility for high throughput can easily be envisaged through massive device parallelization, facilitated by the low device cost (typically $\sim \text{US\$1/device}$). Alternatively, single or multiple devices can be mounted on a spray head for fast simultaneous exfoliation and deposition over large coverage areas on a variety of arbitrary surfaces, an example of which is shown on a 4-inch wafer in Figure 4c,d. Such a versatile and facile spray coating method is extremely useful, for example, for the production of nanostructured TMD substrates as electrodes for enhancing the catalytic activity of hydrogen evolution

reactions (Figure S6, Supporting Information), or for the development of high speed, low power and high efficiency electronic circuits and optical elements.

Experimental Section

Device fabrication: HYDRA nebulization devices, on which surface reflected bulk waves—a hybrid surface and bulk electromechanical wave—propagate as an energy source to induce the nebulization of a liquid, were fabricated by patterning 40 interdigital transducer (IDT) finger pairs comprising 10 nm chromium and $1.5 \mu\text{m}$ aluminum films with 3.9 mm aperture widths on a $500 \mu\text{m}$ thick 128°-YX double-sided polished single-crystal piezoelectric lithium niobate (LiNbO_3) substrate (Roditi Ltd., London, UK) using UV lithography. In the cases where it was desired for the electric field to be suppressed, a thin 15 nm film of gold screening layer atop the device was sputter coated (SPI-Module Sputter Coater, Structure Probe Inc., West Chester, PA, USA). The acoustic waves were then excited on the substrate by applying a sinusoidal electrical input at the resonant

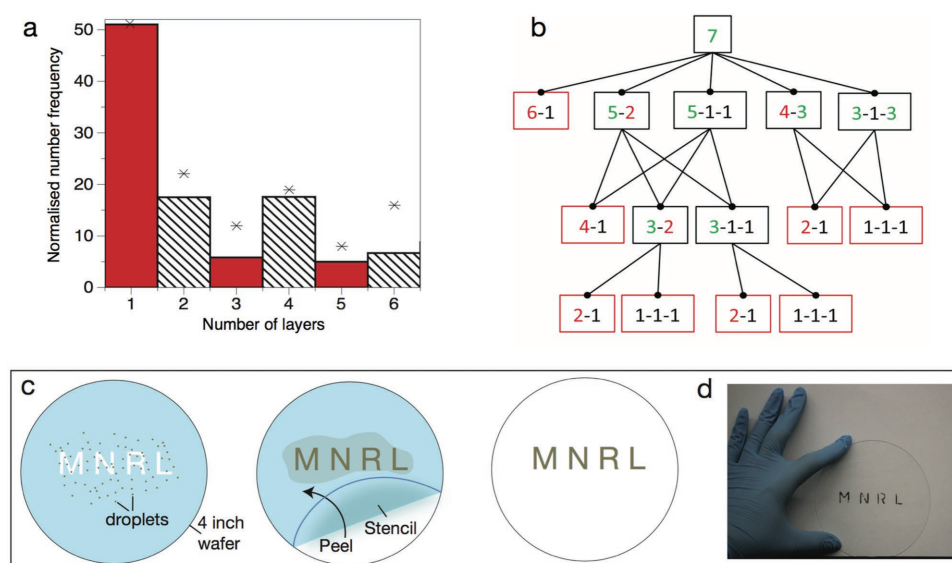


Figure 4. a) Experimental (data points marked by the asterisks) and theoretical distributions (histogram) showing the normalized frequency of obtaining a quasi-2D MoS₂ nanosheet with n numbers of layers. b) Decision tree showing the possible pathways of exfoliating a seven-layer MoS₂ flake in the simulations. Flakes with odd numbers of layers, being piezoelectric, are exfoliated into thinner layers under the applied electric field whereas flakes with even numbers of layers, being nonpiezoelectric, are not exfoliated. c) Schematic illustration of the process involved in simultaneously exfoliating 3D bulk MoS₂ and spray-coating an example pattern of the quasi-2D MoS₂ nanosheets that are produced onto a 4-inch wafer with the aid of a stencil. d) Image of the spray-coated pattern, demonstrating the possibility of a versatile and facile technique for rapid concurrent exfoliation and deposition of arbitrary patterns.

frequency f to the IDTs with a signal generator (SML01; Rhode & Schwarz, North Ryde, NSW, Australia) and amplifier (LYZ-22+, Mini Circuits, Brooklyn, NY, USA), and characterized using laser Doppler vibrometry (UHF-120; Polytec GmbH, Waldbronn, Germany) scans. f is related to the acoustic wavelength λ by $f = c/\lambda$, wherein c is the speed at which the acoustic wave propagates in LiNbO₃; λ is set by the pitch of the interdigitated fingers that make up the IDT electrodes (specifically, four times the finger width and gap). In this work, $f = 30$ MHz.

Exfoliation of MoS₂ and Graphite: 500 mg MoS₂ (6 μ m, 99.9% purity (US1089M, CAS: 1317-33-5); US Research Nanomaterials Inc., Houston, TX, USA), WS₂ (2 μ m, 99.9% purity (243639, CAS: 12138-09-9); Sigma-Aldrich Pty. Ltd., Sydney, NSW, Australia), or graphite (+100 mesh (332461, CAS: 7782-42-5); Sigma-Aldrich Pty. Ltd., Sydney, NSW, Australia) was added to 2% Tween 20 (polyethylene glycol sorbitan monolaurate (P1379, CAS: 9005-64-5); Sigma-Aldrich Pty. Ltd., Sydney, Australia) in 1000 mL deionized water (Milli-Q 18.2 M Ω cm, Merck Millipore, Bayswater, VIC, Australia) to create a 0.5 mg mL⁻¹ suspension of MoS₂ or graphite. The mixture was agitated at 700 rpm and maintained at 80 °C for 24 h, and subsequently left to cool to room temperature, although it was found that this lengthy procedure had little effect on the final exfoliation outcome and could be omitted. The freshly prepared MoS₂, WS₂, or graphite solution was then placed in a 2 mL microcentrifuge tube (Eppendorf South Pacific Pty. Ltd., North Ryde, NSW, Australia), within which a wick comprising a short piece of hand-rolled tissue paper was immersed to act as a fluid conduit from the reservoir to the edge of the device. Upon excitation of the acoustic wave, the MoS₂, WS₂, or graphite suspension was drawn through the wick to the device's edge, where it immediately nebulized into aerosol droplets, within which the exfoliated MoS₂, WS₂, or graphite flakes were trapped. For each run, the suspension was nebulized for 2 min. The droplets and hence the nanosheets were collected as they deposited on a 2 cm \times 2 cm cut silicon plate mounted 5 cm above the device. The water from the deposited droplets was then completely evaporated at 100 °C, leaving behind the nanosheets on the collector plate for subsequent characterization. To quantify the overall yield and nebulization rate,

the acoustic device was weighed before and after nebulization using a microbalance (XP56; Mettler Toledo Ltd., Port Melbourne, VIC, Australia). The monolayer yield, on the other hand, was estimated by collecting the nebulized MoS₂ in a 10 mL Falcon tube, which was subsequently weighed, followed by centrifugation at 7000 rpm for 20 min to separate the exfoliated layers from the bulk. The exfoliated supernatant was then dried at 110 °C and reweighed.

Materials Characterization: The MoS₂ nanosheets that were collected were first characterized using contact mode AFM (Multimode 8 with PeakForce Tunnelling (TUNA) module; Bruker Corp., Santa Barbara, CA, USA) and HRTEM (Tecnai F20, FEI, Hillsboro, OR, USA) with an accelerating voltage of 200 kV. The AFM images were first flattened at a z-threshold of 0.5 nm from which layer thickness and lateral size distributions across 512 bins were acquired by analyzing at least 200 flakes using the supplied software (NanoScope, v6.13, Bruker Corp., Santa Barbara, CA, USA). Raman spectroscopy was conducted with an excitation laser line of 532 nm (10 mW, 200/2000 cm⁻¹ acquisition range; Renishaw Oceania Pty. Ltd., Mulgrave, VIC, Australia). For UV-vis characterization, optical excitation was measured in quartz cuvettes on a UV-vis spectrophotometer (Cary 50 UV-Vis; Varian Inc., Santa Clara, CA, USA) with a path length of 1 cm. Powder XRD (D8 Advance, Bruker Pty. Ltd., Preston, VIC, Australia) was conducted with Cu K α radiation at 40 mA and 40 kV ($\lambda = 1.54$ Å) at a scan rate of 2° min⁻¹, step size of 0.02°, and a 2θ range of 6°–90° from which the average crystallite size can be calculated using the modified Scherrer equation.

Theoretical Calculations: To analyze the outcomes, spin-dependent hybrid density functional theory (DFT) simulations were conducted. This was performed using the Gaussian basis set ab initio package CRYSTAL14,^[18] with a B3LYP hybrid exchange-correlation functional.^[19] The calculation was augmented with an empirical London-type correction to the energy in order to incorporate dispersion contributions for the overall energy. The correction term was that proposed by Grimme^[20] and had been successfully used with B3LYP to obtain the cohesive energies.^[21] Durand Effective Core Pseudopotentials (ECP) for sulfur was used to account for electrons in (1s²2s²2p⁶) and the valance electrons used 1 31G* basis. For molybdenum, a Hay-Wadt small-core ECP was

used to account for the 28 core electrons ($1s^2 2s^2 2p^6 3s^2 3p^6 3d^{10}$) and the valence electrons with a 311-31G basis.^[22] Crystals of one to seven MoS₂ fundamental layers were assembled from a stratified 2H MoS₂ structure, and their bulk energies, subject to a normal electric field applied to its surface, were calculated as described by Grimme.^[20,21] As described previously,^[23,24] $15 \times 15 \times 1$ *k*-point sampling was used to converge the electronic ground state. An estimate for the probability of exfoliating an *n* layer to an $(n - m) + m$ layer slab is given by $P = A \exp(-|\Delta E|/kT)$, wherein *A* is a normalization constant, *k* Boltmann's constant and *T* the absolute temperature. ΔE is the layer exfoliation energy, calculated from $\Delta E = E(m) - [E(n - m) + E(m)]$ for an *n* layer slab separating into $(n - m)$ and *m* layers; *E*(*m*) is the total energy for an *m* layer MoS₂ slab as calculated from DFT (B3LYP).

The data in Figure 4a has been normalized in order to set the frequency of obtaining a nanosheet with five layers equal to 5. This relative proportion was estimated by calculating the probabilities of exfoliation from a seven-layer slab through to a one-layer slab using the equation for ΔE described above. In doing this, all the pathways of exfoliation were examined, as illustrated by the decision tree in Figure 4b. For example, exfoliation could occur starting from a seven-layer slab in the following ways: 7/6-1, 7/5-2, 7/4-3, 7/5-1-1, and 7/3-1-3. The notation 7/6-1 denotes a seven-layer slab splitting into a six-layer and a one-layer slab whereas the notation 7/5-1-1 refers to the exfoliation of a single layer from the top and bottom of a seven-layer slab, resulting in the creation of a five-layer slab and two one-layer planes. As such, the possibility of both single (7/6-1, 7/5-2 and 7/4-3) and double (7/5-1-1 and 7/3-1-1) exfoliation events was accounted for. Once created, new slabs can continue exfoliating to create thinner slabs (Figure 4b). It was assumed that exfoliation is mediated by the electric displacement under an applied electric field. This will occur if a structure is noncentrosymmetric (i.e., it has no inversion symmetry). Simple group theory reveals that odd-numbered layers of MoS₂^[16] possess this property, while even-numbered layers are centrosymmetric and are therefore nonpiezoelectric. As such, it is assumed that once a slab with an even number of layers has been created, no further exfoliation of that slab can occur. Under this assumption it has been determined that there are 19 possible pathways for the exfoliation of a seven-layer slab. For the thinner slabs (i.e., those with one to five layers), successive exfoliation events are required and it is assumed that these are independent events. Therefore, the overall probability is a product of the probabilities for each individual event.

Supporting Information

Supporting Information is available from the Wiley Online Library or from the author.

Acknowledgements

H.A. and A.R.R. contributed equally to this work. A.R.R. is grateful for an RMIT University Vice-Chancellor's Research Fellowship. S.P.R. acknowledges the support of the Australian Research Council (ARC) Centre of Excellence in Exciton Science (CE170100026). L.Y.Y. is funded through an ARC Future Fellowship (FT130100672) and a Discovery Project (DP180102110). The theoretical work was supported by computational resources provided by the National Computational Infrastructure National Facility (NCI-NF) Flagship program and the Pawsey Supercomputer Centre Energy & Resources Merit Allocation Scheme.

Conflict of Interest

The authors declare no conflict of interest

Keywords

2D materials, exfoliation, nebulization, surface acoustic wave microfluidics, transition metal dichalcogenide

Received: August 21, 2017

Revised: February 8, 2018

Published online:

- [1] M. C. Asensio, M. Batzill, *J. Phys.: Cond. Matter* **2016**, *28*, 490301.
- [2] K. S. Novoselov, V. I. Fal'ko, L. Colombo, P. R. Gellert, M. G. Schwab, K. Kim, *Nature* **2012**, *490*, 192.
- [3] J. Zheng, H. Zhang, S. Dong, Y. Liu, C. T. Nai, H. S. Shin, H. Y. Jeong, B. Liu, K. P. Loh, *Nat. Commun.* **2014**, *5*, 2995.
- [4] J. N. Coleman, M. Lotya, A. O'Neill, S. D. Bergin, P. J. King, U. Khan, K. Young, A. Gaucher, S. De, R. J. Smith, I. V. Shvets, S. K. Arora, G. Stanton, H. Y. Kim, K. Lee, G. T. Kim, S. G. Duesberg, T. Hallam, J. J. Boland, J. J. Wang, J. F. Donegan, J. C. Grunlan, G. Moriarty, A. Shmeliov, R. J. Nicholls, J. M. Perkins, E. M. Grieveson, K. Theuvsen, D. McComb, P. D. Nellist, V. Nicolosi, *Science* **2011**, *331*, 568.
- [5] Y. Hernandez, V. Nicolosi, M. Lotya, F. M. Blighe, Z. Sun, S. De, I. T. McGovern, B. Holland, M. Byrne, Y. K. Gun'ko, J. J. Boland, P. Niraj, G. Duesberg, S. Krishnamurthy, R. Goodhue, J. Hutchison, V. Scardaci, A. C. Ferrari, J. N. Coleman, *Nat. Nanotechnol.* **2008**, *3*, 563.
- [6] Z. Yu, Y. Pan, Y. Shen, Z. Wang, Z.-Y. Ong, T. Xu, R. Xin, L. Pan, B. Wang, L. Sun, J. Wang, G. Zhang, Y. W. Zhang, Y. Shi, X. Wang, *Nat. Commun.* **2014**, *5*, 5290.
- [7] C. R. Ryder, J. D. Wood, S. A. Wells, M. C. Hersam, *ACS Nano* **2016**, *10*, 3900.
- [8] T. Wang, R. Zhu, J. Zhuo, Z. Zhu, Y. Shao, M. Li, *Anal. Chem.* **2014**, *86*, 12064.
- [9] A. R. Rezk, J. K. Tan, L. Y. Yeo, *Adv. Mater.* **2016**, *28*, 1970.
- [10] L. Y. Yeo, J. R. Friend, *Annu. Rev. Fluid Mech.* **2014**, *46*, 379.
- [11] X. Ding, P. Li, S.-C. S. Lin, Z. S. Stratton, N. Nama, F. Guo, D. Slotcavage, X. Mao, J. Shi, F. Costanzo, T. J. Huang, *Lab Chip* **2013**, *13*, 3626.
- [12] G. Destgeer, H. J. Sung, *Lab Chip* **2015**, *15*, 2722.
- [13] S. Hu, W. Chen, J. Zhou, F. Yin, E. Uchaker, Q. Zhang, G. Cao, *J. Mater. Chem. A* **2014**, *2*, 7862.
- [14] D. J. Collins, O. Manor, A. Winkler, H. Schmidt, J. R. Friend, L. Y. Yeo, *Phys. Rev. E* **2012**, *86*, 056312.
- [15] Y. Zhan, Z. Liu, S. Najmaei, P. M. Ajayan, J. Lou, *Small* **2012**, *8*, 966.
- [16] E. Varrla, C. Backes, K. R. Paton, A. Harvey, Z. Gholamvand, J. McCauley, J. N. Coleman, *Chem. Mater.* **2015**, *27*, 1129.
- [17] A. R. Rezk, O. Manor, J. R. Friend, L. Y. Yeo, *Nat. Commun.* **2012**, *3*, 1167.
- [18] R. Dovesi, R. Orlando, A. Erba, C. M. Zicovich-Wilson, B. Civalieri, S. Casassa, L. Maschio, M. Ferrabone, M. De La Pierre, P. D'Arco, Y. Noël, M. Causà, M. Rérat, B. Kirtman, *Int. J. Quantum Chem.* **2014**, *114*, 1287.
- [19] A. D. Becke, *J. Chem. Phys.* **1993**, *98*, 5648.
- [20] S. Grimme, *J. Comput. Chem.* **2006**, *27*, 1787.
- [21] B. Civalieri, C. M. Zicovich-Wilson, L. Valenzano, P. Ugliengo, *CrytEngComm* **2008**, *10*, 405.
- [22] F. Corà, A. Patel, N. M. Harrison, C. Roetti, C. R. A. Catlow, *J. Mater. Chem.* **1997**, *7*, 959.
- [23] K. J. Berean, J. Z. Ou, T. Daeneke, B. J. Carey, E. P. Nguyen, Y. Wang, S. P. Russo, R. B. Kaner, K. Kalantar-zadeh, *Small* **2015**, *11*, 5035.
- [24] J. Z. Ou, W. Ge, B. Carey, T. Daeneke, A. Rotbart, W. Shan, Y. Wang, Z. Fu, A. F. Chrimes, W. Wlodarski, S. P. Russo, Y. X. Li, K. Kalantar-zadeh, *ACS Nano* **2015**, *9*, 10313.